IJMMM International Journal of Minerals, Metallurgy and Materials 矿物冶金与材料学报（英文版）

Mechanical properties and interfacial characteristics of 6061 Al alloy plates fabricated by hot-roll bonding

Zongan Luo, Xin Zhang, Zhaosong Liu, Hongyu Zhou, Mingkun Wang, and Guangming Xie

Cite this article as:
Zongan Luo, Xin Zhang, Zhaosong Liu, Hongyu Zhou, Mingkun Wang, and Guangming Xie, Mechanical properties and interfacial characteristics of 6061 Al alloy plates fabricated by hot-roll bonding, *Int. J. Miner. Metall. Mater.*, 31(2024), No. 8, pp. 1890-1899. https://doi.org/10.1007/s12613-023-2801-8

View the article online at SpringerLink or IJMMM Webpage.

INTERNATIONAL JOURNAL OF
Minerals, Metallurgy and Materials

Volume 31, Number 8, August 2024
Page 1890

Research Article

https://doi.org/10.1007/s12613-023-2801-8

Mechanical properties and interfacial characteristics of 6061 Al alloy plates fabricated by hot-roll bonding

Zongan Luo, *Xin Zhang*✉, *Zhaosong Liu*, *Hongyu Zhou*, *Mingkun Wang*, *and Guangming Xie*

State Key Laboratory of Rolling and Automation, Northeastern University, Shenyang 110819, China
(Received: 15 August 2023; revised: 5 November 2023; accepted: 28 November 2023)

Abstract: This work aims to investigate the mechanical properties and interfacial characteristics of 6061 Al alloy plates fabricated by hot-roll bonding (HRB) based on friction stir welding. The results showed that ultimate tensile strength and total elongation of the hot-rolled and aged joints increased with the packaging vacuum, and the tensile specimens fractured at the matrix after exceeding 1 Pa. Non-equilibrium grain boundaries were formed at the hot-rolled interface, and a large amount of Mg_2Si particles were linearly precipitated along the interfacial grain boundaries (IGBs). During subsequent heat treatment, Mg_2Si particles dissolved back into the matrix, and Al_2O_3 film remaining at the interface eventually evolved into MgO. In addition, the local IGBs underwent staged elimination during HRB, which facilitated the interface healing due to the fusion of grains at the interface. This process was achieved by the dissociation, emission, and annihilation of dislocations on the IGBs.

Keywords: 6061 Al alloy; hot-roll bonding; vacuum; mechanical properties; interfacial grain boundaries

1. Introduction

Due to good specific strength, corrosion resistance, weldability, and formability, light alloys represented by 6xxx Al alloy are widely used in aerospace, high-speed ships, construction profiles and other fields [1–2]. The corresponding key components often need to be prepared using large Al alloy ingots with fine grains and uniform composition. However, defects such as severe macro-segregation, porosity, and cracks often occur in extra-large ingots produced using traditional methods of direct chill (DC) casting, which seriously reduces the yield and comprehensive performance of Al alloys [3–5]. And these ingots require prolonged homogenization annealing to eliminate dendrite segregation and extensive milling after subsequent hot rolling due to the crocodile mouth [6], which results in higher energy consumption and lower yield.

Currently, solid phase bonding technology has been widely used in the industrial field [7–8], and high-quality heavy forgings and ultra-heavy steel plates have been successfully produced by hot-compression bonding (HCB) [9–10] and vacuum cladding rolling (VCR) [11], i.e., the preparation of heavy plates or forgings using solid phase bonding of thin plates for thickening. For Al alloys, Hazelett continuous casting direct rolling (CCDR) process has been able to produce continuous casting billets with a thickness of about 19 mm after years of research and development [12–13]. Compared to traditional DC casting, defects such as macroscopic segregation, porosity and cracks can be effectively avoided because the cooling rate from the surface to the core is more uniform. Moreover, the thin plates produced by CCDR do not require a homogenization process and extensive milling, which greatly reduces the production cost and energy consumption of Al alloy thin plates [12,14]. Based on the above technological achievements, this study introduced hot-roll bonding (HRB) into the field of Al alloy preparation, i.e., thick Al plates were prepared by roll-bonding on continuous casting billets. It is worth noting that the Al surface was extremely susceptible to the formation of oxide film that were highly adhesive, chemically stable and insoluble in the aluminum substrate, which thickened rapidly with increasing temperature [15]. Tang *et al*. [16] conducted friction-based additive manufacturing on Al–Mg–Si alloy under atmospheric pressure and found obvious weak-bonding defects at the interface. Therefore, vacuum conditions played an important role in inhibiting the thickening of surface oxide films. For this issue, vacuum friction stir welding (FSW) equipment has been developed for vacuum packaging due to the poor performance of electron beam welding of Al alloys [17]. In fact, excessive vacuum conditions can lead to higher process costs, so it is necessary to carry out HRB experiments at different vacuum conditions to determine a relatively suitable process window.

For the solid phase bonding of Al alloys, many scholars have conducted related studies. Xu *et al*. [18] performed hot pressing bonding on 2A12 Al alloy and found that the inter-

✉ Corresponding author: Xin Zhang E-mail: zx2017neu@163.com

face healing was achieved by dynamic recrystallization (DRX) induced by the migration of interfacial grain boundaries (IGBs). Zhang *et al*. [19] stated that discontinuous dynamic recrystallization (DDRX) and geometric dynamic recrystallization (GDRX) had a positive effect on interface healing during vacuum roll cladding of 7050 Al alloy. Xu *et al*. [20] also reported that DDRX induced by grain boundaries (GBs) bulging or particle-stimulated nucleation contributed to interface healing of 2196 Al alloy during HCB. Yu *et al*. [21] found that the interface bonding effect of 6063 Al alloy was positively correlated with hot-pressing temperature, and the optimal bonding effect was obtained at 530°C. Furthermore, Xie *et al*. [10] found that the bonding interface of 316LN stainless steel was gradually eliminated during HCB, followed by the fusion of grains on both sides of the interface, which meant that the healing of the interface originated from the elimination of IGBs. Therefore, it is necessary to investigate the interface healing mechanism during HRB of 6061 Al alloy.

In addition, 6061 aluminum alloy is a heat treatable strengthening alloy, and the corresponding aging precipitation sequence is as follows: SSSS (super saturated solid solution) → Atomic clusters (Mg, Si) → GP zones (nano-precipitation phase) → β″ (Mg_5Si_6) [22] → β′ (Mg_9Si_5) [23] → β (Mg_2Si, equilibrium phase) [24]. During hot rolling, the second-phase particles in the matrix are heavily precipitated and coarsened, losing the strengthening effect on the matrix. Solution and aging treatments are required to regulate the size, morphology and quantity of strengthening phase particles in the matrix to further regulate the comprehensive performance of the Al alloy plate after hot rolling [25]. Therefore, it is also necessary to study the microstructure and mechanical properties of the aged interface of 6061 Al alloy.

In this work, 6061 Al alloy was subjected to HRB, solution and aging treatment under different vacuum, and the microstructure evolution and mechanical properties at the interface of Al alloy plates were investigated.

2. Experimental

6061-T6 Al alloy plates with the dimensions of 250 mm × 250 mm × 25 mm were used in this work, and chemical compositions of the materials are given in Table 1. Fig. 1(a) shows the schematic of HRB. Surface treatment must be carried out before symmetrical assembly to expose the fresh metal. The 3D surface topography of the treated plates is shown in Fig. 1(b), and the corresponding roughness value (R_a) was 0.53 μm. The treated plates were assembled on the mechanical device inside the vacuum cabin [19] and welded under different vacuum (10^5, 10^3, 1, and 10^{-2} Pa), as shown in Fig. 1(c). Subsequently, HRB with a rolling reduction of 80% was carried at 530°C. The solution and aging treatment process was 540°C × 1 h + 177°C × 8 h. Schematic of sampling location and tensile sample shape on hot-rolled and aged plates is shown in Fig. 1(d).

Table 1. Composition of materials used wt%

Mg	Cu	Si	Fe	Ni	Cr	Mn	Zn	Ti
1.02	0.245	0.688	0.459	0.31	0.23	0.12	0.08	0.03

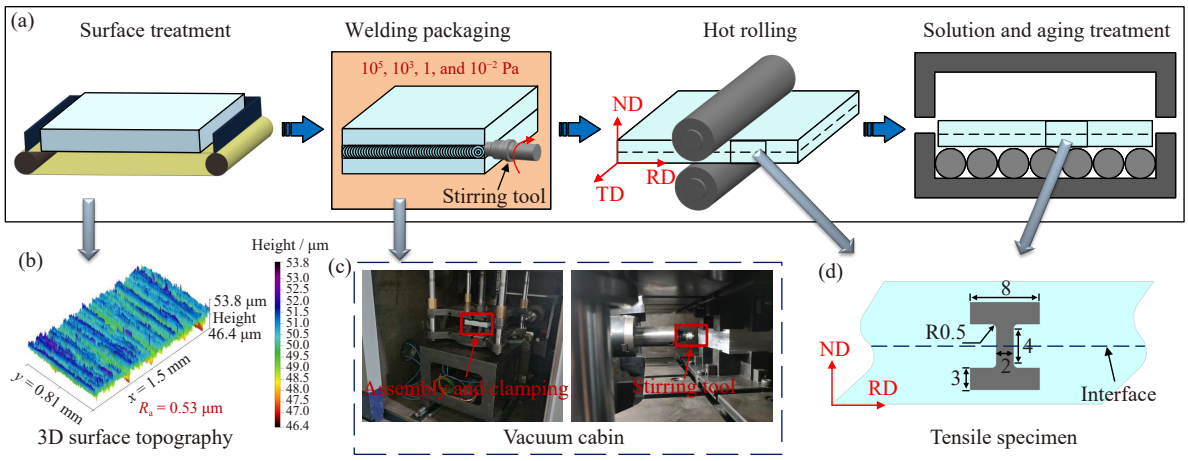

Fig. 1. (a) Schematic of HRB, (b) 3D surface topography after surface treatment, (c) assembly and welding in vacuum cabin, and (d) schematic of sampling location and tensile sample shape.

The samples were cut at the interface of the hot-rolled and aged plates using wire electrical discharge machining, followed by standard metallographic procedures. The bonding zone was observed using OLYMPUSDSX500 optical microscope (OM) and electron probe micro-analyzer (EPMA, JXA-8530F, JEOL) after polishing. Phase identification of the hot-rolled and aged samples was done by X-ray diffraction (XRD, PANalytical, XPertpro) with Cu K_α radiation. Furthermore, the high-temperature confocal laser optical microscope (CLOM, VL2000DX-SVF17SP/15FTC) was used to in situ observe the precipitation and dissolution process of Mg_2Si during solution process, and corresponding heating

process was from room temperature to 500°C at 30°C·s^{-1}, then to 540°C at 10°C·min^{-1}, and hold for 5 min. To further investigate interfacial characteristics, EBSD analysis was carried out using a Zeiss ultra-55 scanning electron microscope (SEM) with the step of 0.1 μm.

3. Results and discussion

3.1. Evolution of interfacial microstructures

Fig. 2 shows cross-sectional OM images of the hot-rolled and aged interface at different vacuum. It can be seen that there are discontinuous gaps and obvious inclusion defects at atmospheric pressure as the joints do not achieve complete physical contact, which leads to the unhealed interface, as shown in Fig. 2(a) and (b). When the vacuum increased to 10^3 Pa, local healing occurred at the interface, although the bonding interface still showed obvious traces (Fig. 2(c) and (d)). As the vacuum increased to 1 Pa and 10^{-2} Pa, there were fine black precipitation phase particles intermittently distributed along the hot-rolled interface (Fig. 2(e) and (g)). After solution and aging treatment, these precipitated phase particles dissolved back into the matrix and eventually some interfacial products were remained at the interface (Fig. 2(f) and (h)).

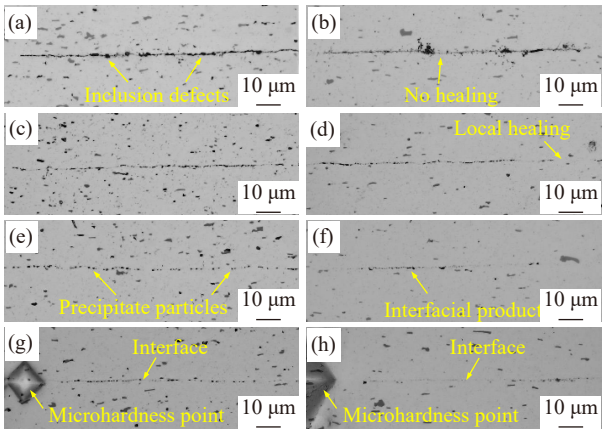

Fig. 2. OM images of the hot-rolled (a, c, e, g) and aged (b, d, f, h) interface at 10^5 Pa (a, b), 10^3 Pa (c, d), 1 Pa (e, f), and 10^{-2} Pa (g, h).

In order to investigate the microstructure evolution of 6061 Al alloy joints, the element distribution and phase composition of the hot-rolled and aged bonding interface at 10^{-2} Pa were detected, and the corresponding results are shown in Fig. 3. Table 2 shows that the energy spectrum results of the corresponding points in the hot-rolled microstructure. Many elliptical black granular precipitates distributed intermittently along the hot-rolled bonding interface (about 1 μm along RN and 0.6 μm along ND), as shown in Fig. 3(a), and the energy spectrum results indicated that such precipitates were rich in Mg, O, and Si elements. In addition, it can be seen that there were also black precipitates with similar morphology, size, and element distribution in the matrix, indicating that the precipitates at the interface were the same as the black precipitated particles in the matrix during HRB. The aged interface showed a linear healing interface locally, and the precipitated particles at the interface have completely disappeared (Fig. 3(b)), suggesting that the precipitated phase at the hot-rolled interface dissolved during the subsequent heat treatment process.

XRD pattern at the hot-rolled and aged interface at 10^{-2} Pa was shown in Fig. 4, and the corresponding results indicated that there were mainly three phases in the hot-rolled microstructure (Fig. 4(a)), namely α-Al, Mg_2Si (β), and Mg_5Si_6 (β″). Qian *et al*. [22] analyzed the formation mechanism of β″ phase through transmission electron microscope (TEM) and first principles calculations, and found that β″ phase was only maintained at the nanoscale. Therefore, the larger black particle phase precipitated at the interface was Mg_2Si (Fig. 3(a)). During the sample preparation process, Mg_2Si phase absorbed O from the air due to its high Mg-rich content, resulting in a higher content of O in EDS detection results, and Peng *et al*. [2] also found a similar phenomenon. The white particle phase in the hot-rolled matrix was an insoluble impurity phase contained Fe element (Fig. 3(a)), i.e., α-Al(Mn, Fe)Si, which was not detected by XRD due to its relatively low content. The element distribution at the aged interface indicated that the interface contained trace amounts of Mg and O elements (Fig. 3(b)), indicating that Al_2O_3 at the interface eventually evolved into Mg-containing oxides.

The ΔG–T relationship in Fig. 5(a) indicates the oxidation

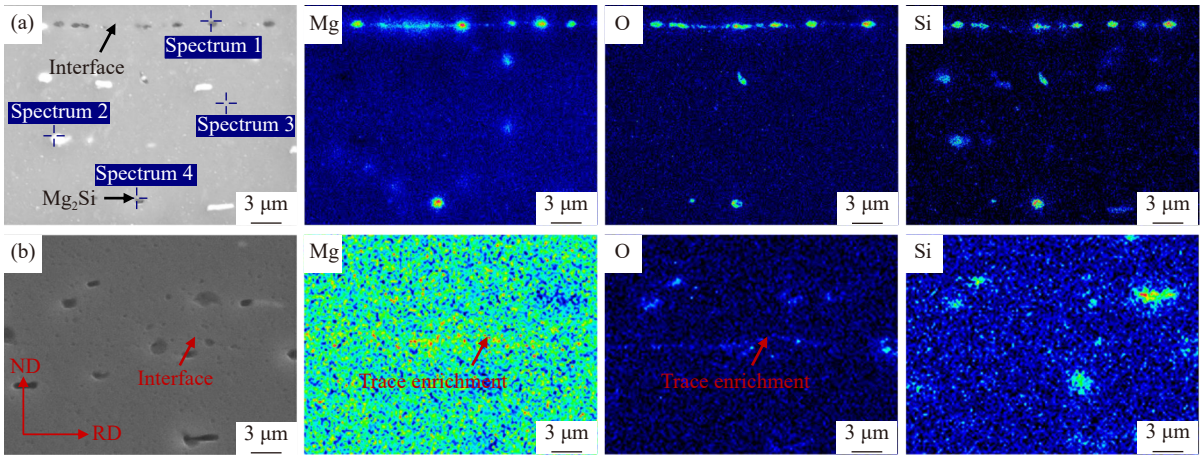

Fig. 3. Element distribution at the hot-rolled (a) and aged (b) interface at 10^{-2} Pa.

Table 2. Energy dispersive spectroscopy (EDS) analysis (wt%) on the selected positions in Fig. 3

Spectrum	Al	Mg	Si	O	Mn	Fe	Identification
1	84.77	4.03	4.92	5.90	0.38	0	Mg_2Si
2	85.31	0	3.61	0	2.75	8.33	α-Al(Mn, Fe)Si
3	98.47	0.93	0.60	0	0	0	Matrix
4	84.42	3.74	5.39	6.10	0.35	0	Mg_2Si

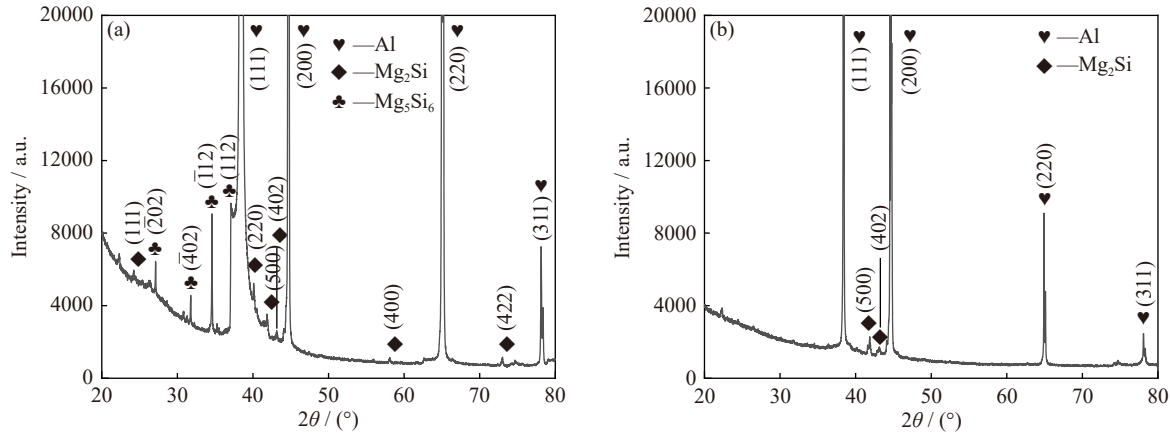

Fig. 4. XRD pattern at the hot-rolled (a) and aged (b) interface at 10^{-2} Pa.

reactions of the corresponding metals can all proceed spontaneously due to $\Delta G < 0$ [26–27]. During solid-state bonding, the oxide layer at the interface is amorphous Al_2O_3 with a thickness of about 5–10 nm. According to the theory of selective oxidation, the greater the affinity with O, the more easily oxides can be formed [26]. Therefore, amorphous Al_2O_3 film can react with Mg to form crystalline MgO as per the chemical reaction (1) in the presence of Mg in the alloy [28]. Panda *et al*. [29–30] investigated the chemical composition of the oxide film on the surface of Al–Mg alloys using real-time *in situ* spectroscopic ellipsometry (RISE) and angle-resolved X-ray photoelectron spectroscopy (AR-XPS), and quantitatively confirmed that Al_2O_3 would gradually evolve into MgO in the range of 125–200°C. In addition, MgO further evolved into $MgAl_2O_4$ spinel with Al_2O_3 as per the chemical reaction (2) [31]. ΔG–T relationship about Al_2O_3 in the range of 100–700°C is shown in Fig. 5(b) [27]. However, Si *et al*. [31] revealed that the complete evolution of Al_2O_3 to $MgAl_2O_4$ spinel requires a temperature of 1550°C. However, the high-temperature treatment process involved in this experiment did not exceed 540°C. Therefore, the final evolution product (Mg-containing oxides) at the interface should be MgO (Fig. 3(b)). And this result and the corresponding evolution process have been confirmed by many researchers [27–28,32]. However, due to the extremely low content of MgO, only two phases were detected in the aged microstructure by XRD (Fig. 4(b)), namely α-Al, Mg_2Si (β).

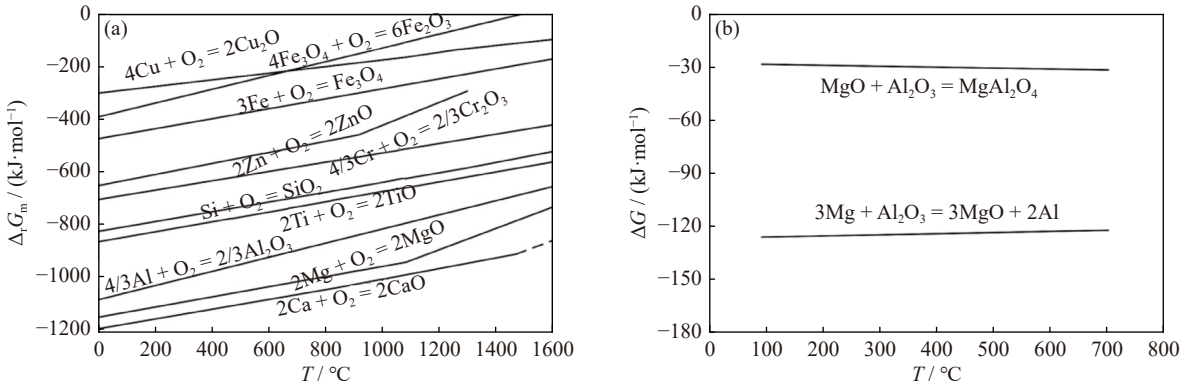

Fig. 5. The ΔG–T relationship curves of (a) oxidation reactions and (b) Al_2O_3 evolution reactions [27]. Reprinted from *Mater. Sci. Eng. A*, 860, X Zhang, Z. A. Luo, Z.S. Liu, *et al*, Interfacial oxide evolution and mechanical properties of 7050 aluminum alloy clad plates during solution and aging process, 144310, Copyright 2022, with permission from Elsevier.

$$3Mg + Al_2O_3 \rightarrow 3MgO + 2Al \quad (1)$$

$$MgO + Al_2O_3 \rightarrow MgAl_2O_4 \quad (2)$$

To investigate the evolution process of precipitate (β) at the interface (marked by microhardness points), high temperature in-situ observation was conducted on the aged joint pre-

pared at 10^{-2} Pa, as shown in Fig. 6. The results show that it is relatively difficult to identify the bonding interface around 200°C (Fig. 6(a)), and intermittently distributed light gray precipitates gradually appeared at the interface after reaching 470°C (Fig. 6(b)). Subsequently, the precipitated phase gradually became clear and distributed along the interface in the form of black particles (Fig. 6(c)). Dolan *et al*. [33] reported that the quenching sensitivity region range of 6061 Al alloy was 250–450°C, which meant that β phase would precipitate and grow rapidly within this temperature range. However, the coarsening temperature of β phase at the interface was relatively high in this experiment, which may be due to the lag of the actual temperature of the sample caused by the rapid heating rate. This indicated that the bonding interface of the 6061 Al alloy formed the so-called "non-equilibrium" GBs [34], namely IGBs, during HRB. Such non-equilibrium GBs served as rapid diffusion paths of solute atoms [35] and provided nucleation sites for β phase. During the hot rolling and cooling processes, the solute atoms on both sides of the interface underwent strong segregation at IGBs [36], which promoted the formation and growth of β phase. During the solution process, the solubility of the alloy increased with the increasing temperature, and β phase at the interface gradually dissolved back into the matrix (Fig. 6(d)).

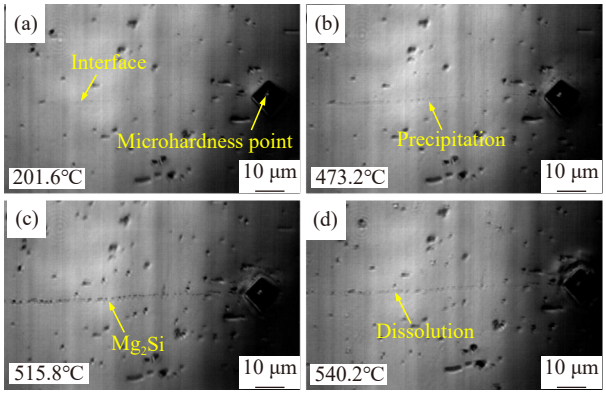

Fig. 6. *In-situ* precipitation and dissolution process of Mg_2Si at the interface: (a, b) below 500°C and (c, d) above 500°C.

3.2. EBSD analysis of the IGBs

To further investigate the bonding behavior of 6061 Al alloy during HRB, the grain structure of the hot-rolled interface (marked by microhardness points) was analyzed, and the corresponding EBSD results are shown in Fig. 7. From inverse pole figure (IPF) map (Fig. 7(a)), it can be seen that the hot-rolled grains were significantly elongated, mainly in [101] orientation, and complete healing occurred at the local bonding interface, i.e., IGBs disappeared and the grains merged, as shown in region 4. Relevant literature indicated that DDRX and GDRX mechanisms contributed significantly to the solid-phase bonding of Al alloys, mainly manifested in the migration and elimination of IGBs [19–20,37]. Therefore, it is necessary to study the DRX behavior at the hot-rolled interface. Grain orientation spread (GOS) can be considered as a measure for dislocation density and strain in individual grains, and grains with GOS value below 1.8 can be defined as recrystallization [38]. From the GOS map (Fig. 7(b)), it can be seen that the grains corresponding to region 4 in Fig. 7(a) was not a recrystallized grain. In addition, although there were DRX grains on both sides of the interface, they did not seem to play a critical role in interface healing, suggesting that another healing mechanism might exist in the HRB process of 6061 Al alloy.

In this study, grain boundaries within 2° to 10°, 10° to 15°, and 15° to 60° were defined as low angle grain boundaries

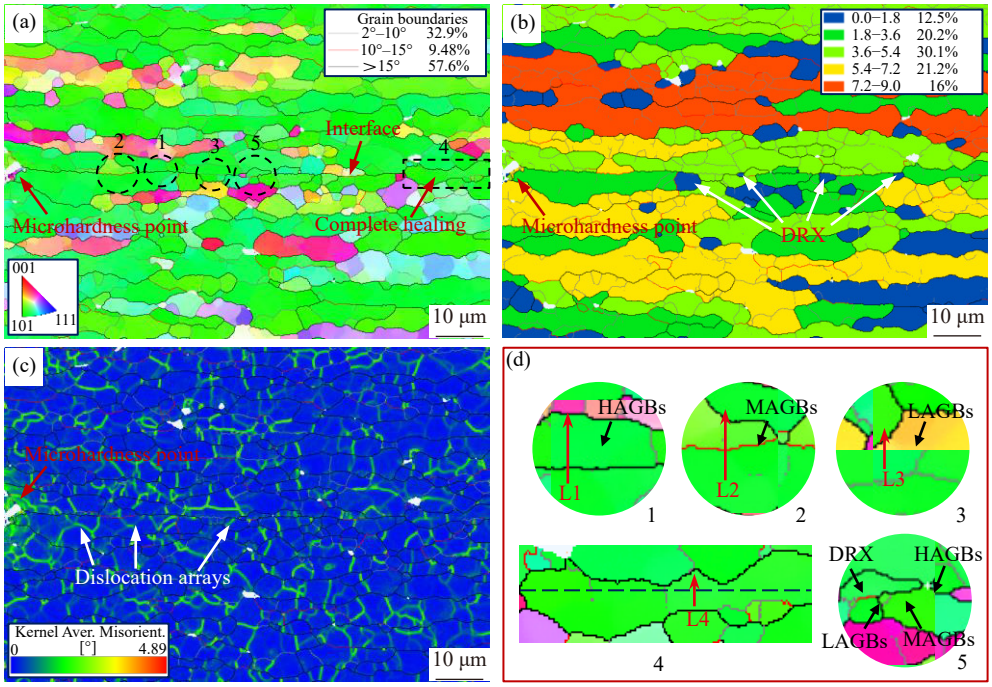

Fig. 7. IPF maps (a), GOS maps (b), and KAM maps (c) at the hot-rolled interface at 10^{-2} Pa, the enlarged image (d) of some bonding areas in (a).

(LAGBs, gray), middle angle grain boundaries (MAGBs, red), and high angle grain boundaries (HAGBs, black), respectively. Kernel average misorientation (KAM) map (Fig. 7(c)) reflected that the strain at the interface was basically the same as that of the matrix. Relevant literature indicated that the main DRX mechanism in 6xxx aluminum alloy was continuous dynamic recrystallization (CDRX) [39], which was mainly manifested as follows: First, a large number of dislocations generated by deformation entangled and formed dislocation arrays and dislocation cells (Fig. 7(c)), which developed into LAGBs in the process of continuous dislocation absorption, and then, LAGBs continued to absorb dislocations to further grew into MAGBs, and finally, subgrains gradually rotated into HAGBs. However, a phenomenon similar to the evolution of reverse CDRX was discovered for the first time at the bonding interface, as shown in Fig. 7(a) and (d), i.e., the bonding interface transformed from HAGBs to MAGBs to LAGBs and finally disappeared completely. The analysis results of the corresponding stages indicated that the misorientation along L1–L4 were about 58.6, 13.9, 8.6, and 0.12, respectively, as shown in Fig. 7(d), indicating that the compatibility between the grains on both sides of the interface gradually increased during HRB. Furthermore, an important evidence was found from Fig. 7(a) and (d) that there were IGBs connected by LAGBs, MAGBs and HAGBs at the interface. This also indicated that the bonding interface underwent staged elimination and eventually formed complete grains, as shown in Fig. 7(a) and (d).

As mentioned earlier, the evolution of grain boundaries during thermal deformation is closely related to dislocations. Dislocations in crystals could be divided into two categories: statistically stored dislocation (SSD) and geometrically necessary dislocation (GND) [40–41]. SSD evolves from random trapping processes, and it is currently difficult to directly obtain its density through relevant tests. GND can adjust the curvature of the crystal lattice and reflect strain gradient field. The relevant literature showed that GND could give a representative trend of the total dislocation density in FCC [41–42]. GND density (ρ_{GND}) measured along L1–L4 is shown in Fig. 8. It can be seen that fluctuations of ρ_{GND} along L2 (MAGBs) and L3 (LAGBs) are more obvious, which indicates that ρ_{GND} on both sides of the interface changes significantly during the staged elimination process of IGBs. Related studies showed that dissociation of HAGBs into LAGBs [43] and annihilation of GBs [44] were both achieved by dislocation emission. The essence was that the full dislocations on the GBs were dissociated into partial dislocations and emitted into the grain, i.e., the new dislocation pairs with opposite Burgers vector were created, then the partial dislocations cancelled out and annihilated with the partial dislocations within the grains or at GBs, i.e., the annihilation of two dislocation pairs was produced by perfect counteracting of the two-opposite-pair Burgers vectors of these two dislocation pairs. Based on the GND distribution results (Fig. 8) at the interface, it can be reasonably inferred that the elimination of IGBs of 6061 Al alloy during HRB

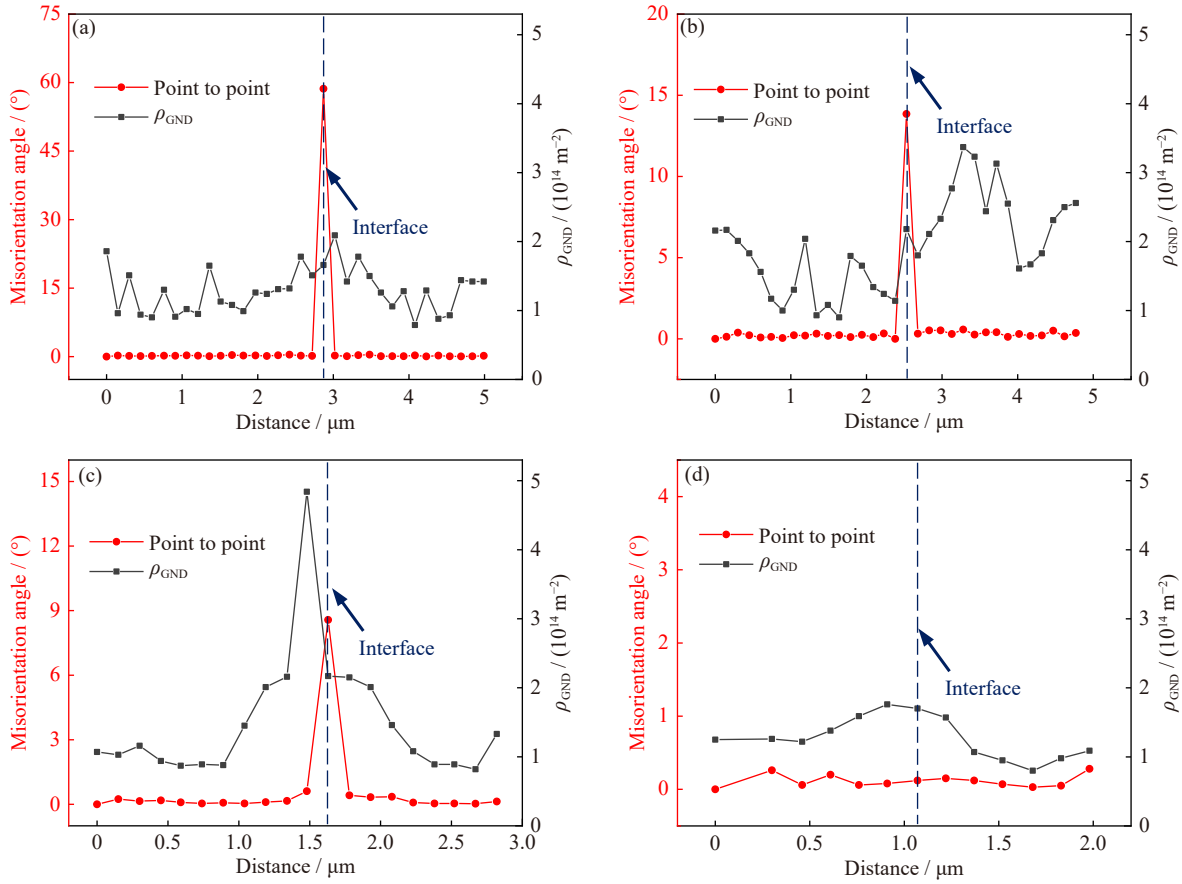

Fig. 8. Misorientation angle and GND density (ρ_{GND}) measured along the lines 'L1' (a), 'L2' (b), 'L3' (c), and 'L4' (d) marked in Fig. 7.

was also achieved by dislocation emission and annihilation. However, due to the effect of CDRX, a large number of dislocations were generated during the thermal deformation of 6xxx Al alloy, resulting in the formation of a large number of substructures. This indicated that the formation and annihilation of GBs (HAGBs) and subgrain boundaries (LAGBs and MAGBs) during HRB was a dynamic process, but the overall trend was that the total amount of GBs and subgrain boundaries was increasing. During this process, the staged elimination of IGBs contributed to interface healing. Pole figures and orientation distribution function (ODF) sections at the hot-rolled interface are shown in Fig. 9. It can be seen that there was a very obvious F texture at the hot-rolled interface.

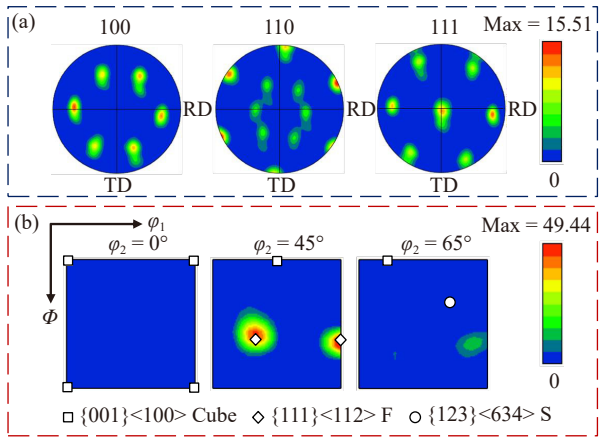

Fig. 9. Pole figures (a) and ODF sections (φ_2 = 0°, 45°, 65°) (b) at the hot-rolled interface at 10^{-2} Pa.

3.3. Mechanical properties of the joints

The engineering stress–strain curves of the bonding joints with different vacuum is shown in Fig. 10, and ultimate tensile strength (UTS) and total elongation (TE) extracted from Fig. 10 are listed in Table 3. It can be seen that UTS and TE of the hot-rolled and aged joints increased with the packaging vacuum. Tensile fracture morphology of the bonding joints (the tensile frontal and profile fracture characteristics are located in the upper right and lower left corners of the images, respectively) at 10^5 Pa and 1 Pa is shown in Fig. 11. At 10^5 Pa, the macroscopic fractures of both hot-rolled and aged joints are relatively flat, with locally smooth areas and small and shallow dimples on the fracture surfaces (Fig. 11(a) and (b)), which indicates weaker bonding effects are obtained. And the EDS results indicate that there is significant oxidation on the fracture surface of the hot-rolled joint at 10^5 Pa. At 1 Pa, both hot-rolled and aged joints underwent significant deformation during the tensile process, with the fracture surface showing large and deep dimples (Fig. 11(c) and (d)). In addition, there are a large number of second phase particles in the dimples of hot-rolled and aged fractures. The EDS results indicate that the particle in the hot-rolled matrix is Mg_2Si phase, and the insoluble impurity phase particle in the aged matrix is $Al_6(Mn, Fe)$ phase. Based on the corresponding tensile curves, it can be seen that under 10^5 and 10^3 Pa conditions, the elongation of the bonded joint is significantly lower, and the fracture mode is brittle fracture. After the vacuum reaches 1 Pa, UTS and TE of the corresponding hot-rolled joints are 163 MPa and 44.9%, respectively. After solution and aging treatment, the strength of the joint increases to 306 MPa, and the corresponding plasticity decreases to 20.9%. The interface still showed good metallurgical bonding effect and ductile fracture occurred. The UTS of T6-AA6061 Al alloy obtained by Nagasai *et al.* [45], Liu *et al.* [1], and Thakur *et al.* [46] was 318 MPa, 301 MPa, and

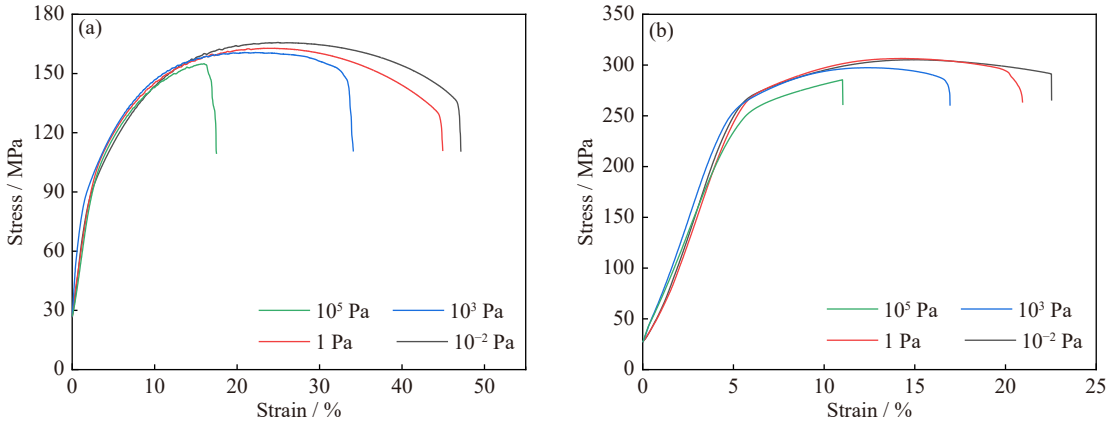

Fig. 10. Stress–strain curves of the hot-rolled (a) and aged (b) joints with different vacuum.

Table 3. UTS and TE extracted from Fig. 10

Vacuum degree / Pa	UTS / MPa		TE / %	
	The hot-rolled	The aged	The hot-rolled	The aged
10^5	155 ± 16	285 ± 36	17.5 ± 11.3	11.0 ± 6.8
10^3	161 ± 12	297 ± 18	34.1 ± 9.7	16.9 ± 5.1
1	163 ± 10	306 ± 15	44.9 ± 6.5	20.9 ± 3.7
10^{-2}	166 ± 10	305 ± 13	47.1 ± 4.3	22.5 ± 2.3

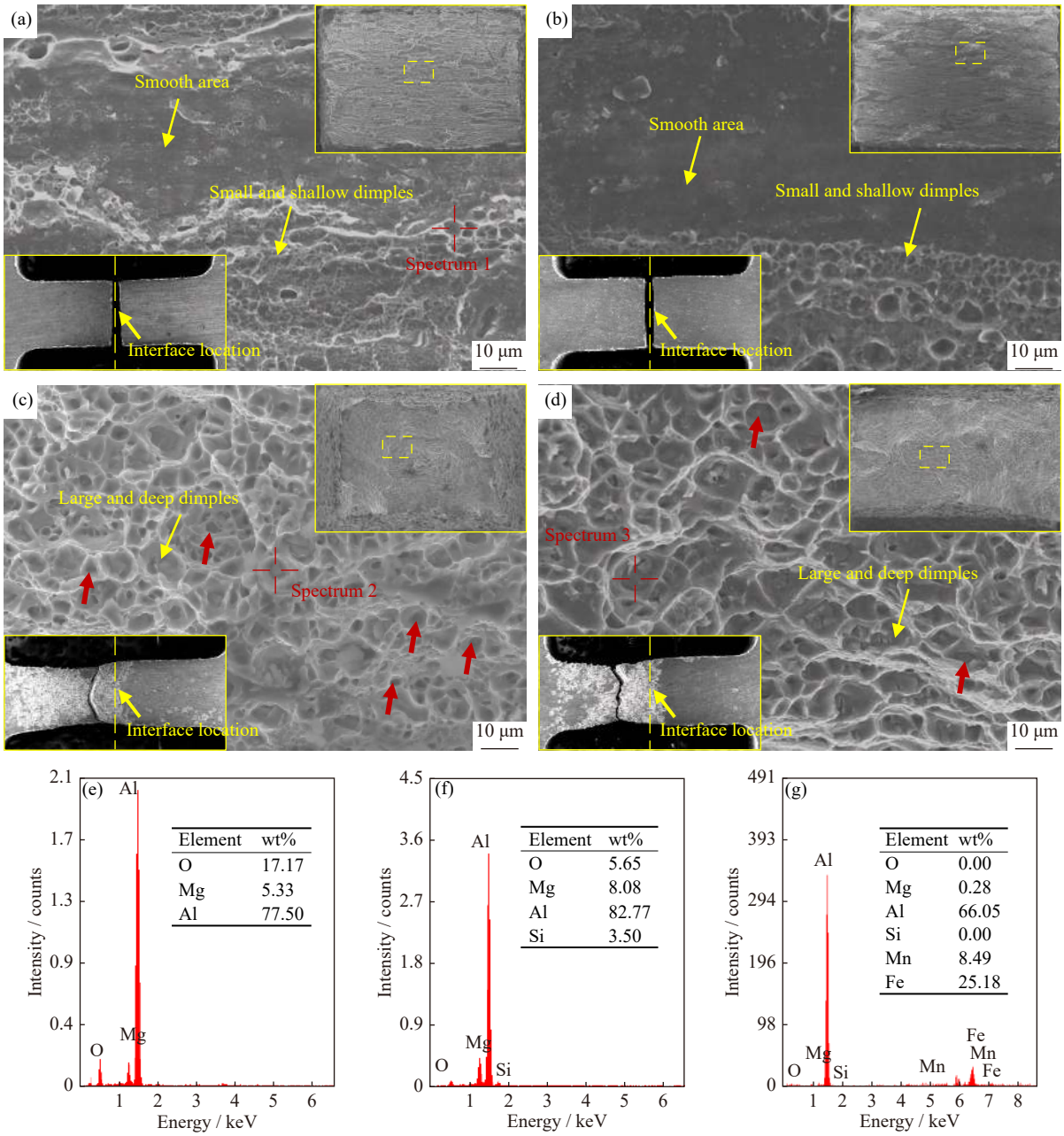

Fig. 11. Tensile fracture morphology and corresponding EDS analysis of the hot-rolled (a, c) and aged (b, d) bonding joints at 10^5 Pa (a, b) and 1 Pa (c, d); (e) spectrum 1, (f) spectrum 2, and (g) spectrum 3.

282 MPa, respectively. Therefore, it is necessary to increase the vacuum condition to more than 1 Pa during HRB of 6061 aluminum alloy.

3.4. Interfacial evolution mechanism

Based on the results described above, the interfacial microstructure evolution of 6061 Al alloy during HRB and heat-treatment can be schematically summarized, as shown in Fig. 12. At 10^5 Pa, there were significant cracks at the bonding interface (Fig. 12(a)). When the vacuum increased to 10^3 Pa, Mg_2Si particles were precipitated along the locally healed interface. However, due to excessive oxidation, the bonding effect at the interface was still poor (Fig. 12(b)), leading to brittle fracture. As the vacuum exceeded 1 Pa, good metallurgical bonding was achieved at the joints due to the effective reduction of oxidation, the hot-rolled bonding interface formed the non-equilibrium GBs, namely IGBs, and Mg_2Si particles were precipitated along the IGBs due to the decrease in solubility during the subsequent cooling process (Fig. 12(c)). In addition, during the hot deformation, the solute atoms have completely dissolved back into the matrix due to the high temperature (530°C), the bonding interface mainly underwent the evolution of grain structure, i.e., part of IGBs transformed from HAGBs to MAGBs to LAGBs, and eventually disappeared completely (Fig. 12(e)), which contributed to the interface healing. This process was achieved by the dissociation, emission, and subsequent annihilation of dislocations on the IGBs. The trace amount of Al_2O_3 film at the interface eventually evolved into MgO during solution and aging treatment (Fig. 12(d)).

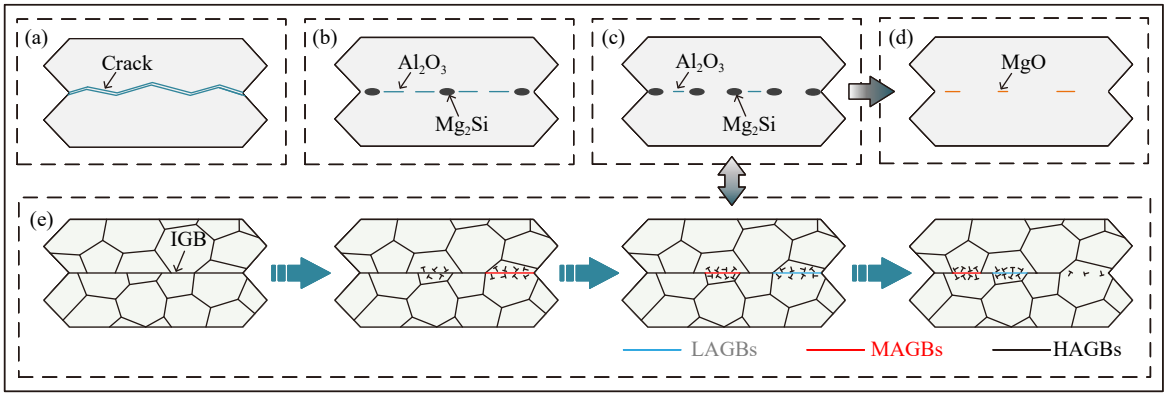

Fig. 12. Schematic of interfacial evolution mechanism: (a) the hot-rolled at 10^5 Pa, (b) the hot-rolled at 10^3 Pa, (c) the hot-rolled over 1 Pa, (d) the aged over 1 Pa, and (e) evolution of grain structure at the interface during HRB over 1 Pa.

4. Conclusions

In this work, mechanical properties and interfacial microstructure evolutions of 6061 Al alloy bonding joints produced by hot-roll bonding based on friction stir welding were investigated. The results can be summarized as follows:

(1) Mechanical properties of the joints produced by HRB increased with the packaging vacuum. At 10^5 and 10^3 Pa, there were obvious inclusion defects at the interface due to excessive oxidation. And the corresponding tensile specimens both fractured at the joints, showing obvious brittle fracture.

(2) After exceeding 1 Pa, metallurgical bonding was achieved at the interface due to a significant reduction in oxidation. And the corresponding hot-rolled and aged specimens both fractured at the matrix with UTS of about 163 and 306 MPa.

(3) After exceeding 1 Pa, local IGBs transformed from HAGBs to MAGBs to LAGBs, and eventually disappeared during HRB, which contributed to the interface healing. This process was achieved by the dissociation, emission, and subsequent annihilation of dislocations on the IGBs.

(4) After exceeding 1 Pa, the hot-rolled interface formed the non-equilibrium GBs. Mg_2Si particles were linearly precipitated along the IGBs during the cooling after rolling, and dissolved into the matrix during solution treatment. The trace amount of Al_2O_3 film remaining at the interface eventually evolved into MgO.

Acknowledgements

This work was financially supported by the National Key Research and Development Program of China (No. 2018YFA0707300) and the Key Research and Development Program projects of Shandong (No. 2020CXGC010304).

Conflict of Interest

All authors declare that they have no financial interests or personal relationships that could have appeared to influence the work reported in this paper.

References

[1] T.S. Liu, F. Qiu, H.Y. Yang, *et al*., Insights into the influences of nanoparticles on microstructure evolution mechanism and mechanical properties of friction-stir-welded Al_{6061} alloys, *Mater. Sci. Eng. A*, 871(2023), art. No. 144929.

[2] C. Peng, G.W. Cao, T.Z. Gu, C. Wang, Z.Y. Wang, and C. Sun, The corrosion behavior of the 6061 Al alloy in simulated Nansha marine atmosphere, *J. Mater. Res. Technol.*, 19(2022), p. 709.

[3] F.B. Meng, H.J. Huang, X.G. Yuan, X.J. Lin, Z.W. Cui, and X.L. Hu, Segregation in squeeze casting 6061 aluminum alloy wheel spokes and its formation mechanism, *China Foundry*, 18(2021), No. 1, p. 45.

[4] Y. Li, H.X. Li, L. Katgerman, Q. Du, J.S. Zhang, and L.Z. Zhuang, Recent advances in hot tearing during casting of aluminium alloys, *Prog. Mater. Sci.*, 117(2021), art. No. 100741.

[5] M. Jolly and L. Katgerman, Modelling of defects in aluminium cast products, *Prog. Mater. Sci.*, 123(2022), art. No. 100824.

[6] P.J. Hao, A.R. He, and W.Q. Sun, Formation mechanism and control methods of inhomogeneous deformation during hot rough rolling of aluminum alloy plate, *Arch. Civ. Mech. Eng.*, 18(2018), No. 1, p. 245.

[7] T.T. Zhang, W.X. Wang, J. Zhang, and Z.F. Yan, Interfacial bonding characteristics and mechanical properties of H68/AZ31B clad plate, *Int. J. Miner. Metall. Mater.*, 29(2022), No. 6, p. 1237.

[8] X. Han, H.T. Zhang, B. Shao, L. Li, K. Qin, and J.Z. Cui, Interfacial characteristics and properties of a low-clad-ratio AA4045/AA3003 cladding billet fabricated by semi-continuous casting, *Int. J. Miner. Metall. Mater.*, 23(2016), No. 9, p. 1097.

[9] B.J. Xie, M.Y. Sun, B. Xu, C.Y. Wang, D.Z. Li, and Y.Y. Li, Dissolution and evolution of interfacial oxides improving the mechanical properties of solid state bonding joints, *Mater. Des.*, 157(2018), p. 437.

[10] B.J. Xie, M.Y. Sun, B. Xu, *et al*., Evolution of interfacial characteristics and mechanical properties for 316LN stainless steel joints manufactured by hot-compression bonding, *J. Mater. Process. Technol.*, 283(2020), art. No. 116733.

[11] G.M. Xie, Z.A. Luo, H.G. Wang, G.D. Wang, and L.J. Wang, Microstructure and mechanical properties of heavy gauge plate by vacuum cladding rolling, *Adv. Mater. Res*., 97-101(2010), p. 324.

[12] R.P. Jiang, W.H. Zhao, L. Zhang, X.Q. Li, and S.K. Guan, Microstructure and corrosion resistance of commercial purity aluminum sheet manufactured by continuous casting direct rolling after ultrasonic melt pre-treatment, *J. Mater. Res. Technol.*,

22(2023), p. 1522.
[13] P.K. Penumakala, A.K. Nallathambi, E. Specht, U. Urlau, D. Hamilton, and C. Dykes, Influence of process parameters on solidification length of twin-belt continuous casting, *Appl. Therm. Eng.*, 134(2018), p. 275.
[14] J.R. Zhao, F.Y. Hung, and B.J. Chen, Effects of heat treatment on a novel continuous casting direct rolling 6056 aluminum alloy: cold rolling characteristics and tensile fracture properties, *J. Mater. Res. Technol.*, 11(2021), p. 535.
[15] M. Akbarifar, M. Divandari, S.M. A. Boutorabi, S.H. Ha, Y.O. Yoon, and S.K. Kim, Short-time oxidation of Al–Mg in dynamic conditions, *Oxid. Met.*, 94(2020), No. 5, p. 409.
[16] W.S. Tang, X.Q. Yang, C.B. Tian, and Y.S. Xu, Microstructural heterogeneity and bonding strength of planar interface formed in additive manufacturing of Al−Mg−Si alloy based on friction and extrusion, *Int. J. Miner. Metall. Mater.*, 29(2022), No. 9, p. 1755.
[17] G.Q. Chen, J.P. Liu, H.Z. Wang, Z.B. Dong, X. Shu, and B.G. Zhang, Underlying cause of the performance deteriorates of Al–Cu–Mg alloy via electron-beam welding and the mechanism of ultrasonic modification, *Sci. Technol. Weld. Joining*, 25(2020), No. 8, p. 653.
[18] D.Z. Xu, L.G. Meng, C.R. Zhang, X. Chen, and X.G. Zhang, Interface microstructure evolution and bonding mechanism during vacuum hot pressing bonding of 2A12 aluminum alloy, *Mater. Charact.*, 189(2022), art. No. 111997.
[19] X. Zhang, Z.A. Luo, G.M. Xie, H. Yu, Z.S. Liu, and J.S. Yang, Interface microstructure and bonding mechanisms of 7050 aluminum alloy thick plates produced by vacuum roll cladding, *Mater. Sci. Eng. A*, 850(2022), art. No. 143582.
[20] X. Xu, X.W. Ma, S.B. Yu, G.Q. Zhao, Y.X. Wang, and X.X. Chen, Bonding mechanism and mechanical properties of 2196 Al-Cu-Li alloy joined by hot compression deformation, *Mater. Charact.*, 167(2020), art. No. 110486.
[21] J.Q. Yu, G.Q. Zhao, X.X. Chen, and M.C. Liang, A comparative study on hot deformation and solid-state bonding behavior of aluminum alloys for the integration of solid-state joining and forming processes, *Int. J. Adv. Manuf. Technol.*, 104(2019), No. 9, p. 3849.
[22] X.M. Qian, Z.D. Wang, Y. Li, Y.F. Wang, and Y. Peng, Formation mechanism of β" -Mg_5Si_6 and its PFZ in an Al-Mg-Si-Mn alloy: Experiment and first-principles calculations, *Mater. Charact.*, 197(2023), art. No. 112617.
[23] R. Vissers, M.A. van Huis, J. Jansen, H.W. Zandbergen, C.D. Marioara, and S.J. Andersen, The crystal structure of the β' phase in Al–Mg–Si alloys, *Acta Mater.*, 55(2007), No. 11, p. 3815.
[24] H. Shishido, Y. Aruga, Y. Murata, C.D. Marioara, and O. Engler, Evaluation of precipitates and clusters during artificial aging of two model Al–Mg–Si alloys with different Mg/Si ratios, *J. Alloys Compd.*, 927(2022), art. No. 166978.
[25] S.J. Yao, Q.H. Tang, J. Yang, *et al*., Microstructural characterization and mechanical properties of 6061 aluminum alloy processed with short-time solid solution and aging treatment, *J. Alloys Compd.*, 960(2023), art. No. 170704.
[26] N. Birks, G.H. Meier, and F.S. Pettit, *Introduction to the High Temperature Oxidation of Metals*, Cambridge University Press, Cambridge, 2006.
[27] X. Zhang, Z.A. Luo, Z.S. Liu, *et al*., Interfacial oxide evolution and mechanical properties of 7050 aluminum alloy clad plates during solution and aging process, *Mater. Sci. Eng. A*, 860(2022), art. No. 144310.
[28] D. Labus Zlatanovic, S. Balos, J.P. Bergmann, *et al*., In-depth microscopic characterisation of the weld faying interface revealing stress-induced metallurgical transformations during friction stir spot welding, *Int. J. Mach. Tools Manuf.*, 164(2021), art. No. 103716.
[29] E. Panda, L.P.H. Jeurgens, and E.J. Mittemeijer, Effect of *in vacuo* surface pre-treatment on the growth kinetics and chemical constitution of ultra-thin oxide films on Al–Mg alloy substrates, *Surf. Sci.*, 604(2010), No. 5-6, p. 588.
[30] D. Ajmera and E. Panda, Thermodynamics of ultra-thin oxide overgrowths on Al–Mg alloys: Role of interface energy, *Corros. Sci.*, 102(2016), p. 425.
[31] Y.C. Si, F. Zhang, X. Li, *et al*., Thermodynamic calculation and microstructure characterization of spinel formation in MgO–Al_2O_3–C refractories, *Ceram. Int.*, 48(2022), No. 11, p. 15525.
[32] D. Labus Zlatanovic, J. Pierre Bergmann, S. Balos, J. Hildebrand, M. Bojanic-Sejat, and S. Goel, Effect of surface oxide layers in solid-state welding of aluminium alloys–review, *Sci. Technol. Weld. Joining*, 28(2023), No. 5, p. 331.
[33] G.P. Dolan and J.S. Robinson, Residual stress reduction in 7175-T73, 6061-T6 and 2017A-T4 aluminium alloys using quench factor analysis, *J. Mater. Process. Technol.*, 153-154(2004), p. 346.
[34] A.A. Nazarov, A.E. Romanov, and R.Z. Valiev, On the structure, stress fields and energy of nonequilibrium grain boundaries, *Acta Metall. Mater.*, 41(1993), No. 4, p. 1033.
[35] T. Fujita, Z. Horita, and T.G. Langdon, Characteristics of diffusion in Al-Mg alloys with ultrafine grain sizes, *Philos. Mag. A*, 82(2002), No. 11, p. 2249.
[36] Y.X. Lai, W. Fan, M.J. Yin, C.L. Wu, and J.H. Chen, Structures and formation mechanisms of dislocation-induced precipitates in relation to the age-hardening responses of Al–Mg–Si alloys, *J. Mater. Sci. Technol.*, 41(2020), p. 127.
[37] L.Y. Zhou, S.B. Feng, M.Y. Sun, B. Xu, and D.Z. Li, Interfacial microstructure evolution and bonding mechanisms of 14YWT alloys produced by hot compression bonding, *J. Mater. Sci. Technol.*, 35(2019), No. 8, p. 1671.
[38] Y. Zhang, J.F. Jiang, Y. Wang, G.F. Xiao, Y.Z. Liu, and M.J. Huang, Recrystallization process of hot-extruded 6A02 aluminum alloy in solid and semi-solid temperature ranges, *J. Alloys Compd.*, 893(2022), art. No. 162311.
[39] J.C. Li, X.D. Wu, L.F. Cao, B. Liao, Y.C. Wang, and Q. Liu, Hot deformation and dynamic recrystallization in Al–Mg–Si alloy, *Mater. Charact.*, 173(2021), art. No. 110976.
[40] J.Y. Zhang, B. Wang, and H. Wang, Geometrically necessary dislocations distribution in face-centred cubic alloy with varied grain size, *Mater. Charact.*, 162(2020), art. No. 110205.
[41] C.Y. Zhu, T. Harrington, G.T. Gray, and K.S. Vecchio, Dislocation-type evolution in quasi-statically compressed polycrystalline nickel, *Acta Mater.*, 155(2018), p. 104.
[42] J.H. Zheng, C. Pruncu, K. Zhang, K.L. Zheng, and J. Jiang, Quantifying geometrically necessary dislocation density during hot deformation in AA6082 Al alloy, *Mater. Sci. Eng. A*, 814(2021), art. No. 141158.
[43] A. Kedharnath, R. Kapoor, and A. Sarkar, Evolution of dislocations and grain boundaries during multi-axial forging of tantalum, *Int. J. Refract. Met. Hard Mater*, 112(2023), art. No. 106120.
[44] Y.J. Gao, C.J. Lu, Z.R. Luo, K. Lin, and C.G. Huang, Phase field crystal simulation of dislocation emission and annihilation at grain boundary, *Chin. J. Nonferrous Met.*, 24(2014), No. 8, p. 2073.
[45] B. Prasanna Nagasai, A. Ramaswamy, and J. Mani, Tensile properties and microstructure of surface tension transfer (STT) arc welded AA 6061-T6 aluminum alloy joints, *Mater. Today Proc.*, 2023. https://doi.org/10.1016/j.matpr.2023.04.576
[46] A. Thakur, V. Sharma, N. Minhas, S. Manda, and V.S. Sharma, Microstructure and mechanical properties of dissimilar friction stir welded joints of laser powder bed fusion processed $AlSi_{10}Mg$ and conventional hot rolled 6061-T6 thin sheets, *Opt. Laser Technol.*, 163(2023), art. No. 109382.